SCIENTIFIC REPORTS

OPEN

The Strain Rate Effect on the Buckling of Single-Layer MoS_2

SUBJECT AREAS:
TWO-DIMENSIONAL MATERIALS
NANOSCALE DEVICES

Jin-Wu Jiang

Shanghai Institute of Applied Mathematics and Mechanics, Shanghai Key Laboratory of Mechanics in Energy Engineering, Shanghai University, Shanghai 200072, People's Republic of China.

Received
24 September 2014
Accepted
10 December 2014
Published
15 January 2015

Correspondence and requests for materials should be addressed to J.-W.J. (jiangjinwu@shu.edu.cn)

The Euler buckling theory states that the buckling critical strain is an inverse quadratic function of the length for a thin plate in the static compression process. However, the suitability of this theory in the dynamical process is unclear, so we perform molecular dynamics simulations to examine the applicability of the Euler buckling theory for the fast compression of the single-layer MoS_2. We find that the Euler buckling theory is not applicable in such dynamical process, as the buckling critical strain becomes a length-independent constant in the buckled system with many ripples. However, the Euler buckling theory can be resumed in the dynamical process after restricting the theory to an individual ripple in the buckled structure.

The buckling critical strain of a thin plate can be described by the Euler buckling theory[1], i.e., $\epsilon_c = -\frac{4\pi^2 D}{C_{11}L^2}$, where D is the bending modulus and C_{11} is the in-plane tension stiffness. L is the length of the plate. The Euler buckling theory was developed for static compression processes. The static compression process is equivalent to molecular dynamics (MD) simulations with extremely low strain rates. Although this theory has been widely used in static mechanical processes, it is still unclear whether the Euler buckling theory is applicable in dynamical compression processes, where the strain rate has important effect on the compression/tension behavior of the system[2]. For instance, it is crucial to apply mechanical strain at a very low strain rate for the study of structure transitions, so that the system has enough time to relax its structure. We thus examine in present work whether the Euler buckling theory is applicable in the dynamical compression process.

We investigate the applicability of the Euler buckling theory using the Molybdenum Disulphide (MoS_2). MoS_2 has attracted considerable attention in recent years on its electronic, thermal, or mechanical properties[3–19]. Different two-dimensional materials (eg. graphene and MoS_2) have complementary physical properties. Therefore, experimentalists have combined graphene and MoS2 in specific ways to create heterostructures that mitigate the negative properties of each individual constituent[20]. However, the temperature change will lead to some mechanical compression/tension on the heterostructure, because of different thermal expansion coefficient of graphene and MoS_2[21]. This thermal-induced mechanical compression will trigger the buckling of some layers in the sandwich structure, as the buckling critical strain is usually very low for layered materials. Hence, it is important to investigate the buckling phenomenon for the single-layer MoS_2 ($SLMoS_2$), which was investigated by only limited works[19].

In this paper, we perform MD simulations to examine the applicability of the Euler buckling theory in the dynamical compression of $SLMoS_2$ at different strain rates. It turns out that the Euler buckling theory is not applicable for longer $SLMoS_2$ at higher strain rates, in which the buckling critical strain becomes length independent. However, the Euler buckling theory will become applicable after restricting it to the individual ripple in the buckled $SLMoS_2$.

Results

The $SLMoS_2$ can be constructed by duplicating a rectangular unit cell of (5.40, 3.12) Å in the two-dimensional plane as shown in Fig. 1. The number of unit cell is n_x and n_y in the armchair and zigzag directions. The length of the $SLMoS_2$ is $5.40 \times n_x$, and its width is $3.12 \times n_y$. We fix $n_y = 10$ for all simulations in present work. The free boundary condition is applied in the out-of-plane direction. We apply the fixed boundary condition in the armchair direction. The periodic boundary condition is applied in the zigzag direction. The $SLMoS_2$ is compressed in the armchair direction. The zigzag direction is kept stress free during compression.

Fig. 2 shows the stress-strain relation for the $SLMoS_2$ with $n_x = 100$, which is compressed at strain rates of $\dot{\epsilon} = 10^9$ s^{-1}, 10^8 s^{-1}, and 10^7 s^{-1}, respectively. A value for the thickness is required for the computation of the

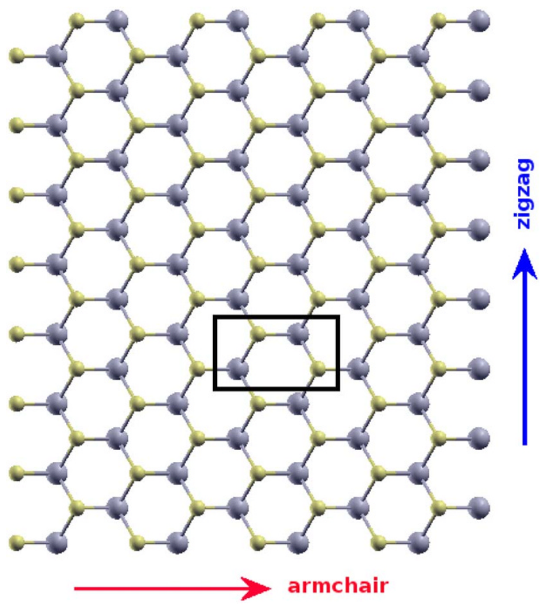

Figure 1 | **Structure for $SLMoS_2$, with (n_x, n_y) = (4, 8).** The unit cell is enclosed by the black rectangular. n_x and n_y are the numbers of the unit cell in the armchair and zigzag directions, respectively.

stress. However thickness is not a well-defined quantity in the quasi-two-dimensional layered materials such as $SLMoS_2$. Hence, we have assumed the thickness of the $SLMoS_2$ to be the space between two neighboring MoS_2 layers in the three-dimensional bulk MoS_2. That is the thickness is chosen as 6.09 Å for $SLMoS_2$. The x-axis in Fig. 2 is the absolute value for the compression strain. The $SLMoS_2$ buckles at the critical strain, at which the stress within the system starts to drop. The critical strain is sensitive to the strain rate, and the buckling critical strain increases sharply with increasing strain rate. This phenomenon is not new and has been reported in our previous work[19]. It has also been observed in the compression of graphene[22].

Insets (from top to bottom) of Fig. 2 illustrate the buckling mode of the $SLMoS_2$, which is compressed with strain rates of $\dot{\epsilon} = 10^9$ s^{-1}, 10^8 s^{-1}, and 10^7 s^{-1}, respectively. An individual ripple in the buckling mode is enclosed by the rectangular. The length of the ripple decreases quickly with increasing strain rate. Normally, the buckling mode follows the shape of the first bending phonon mode in the system, in which only one ripple occurs after buckling. However, if the system is compressed very fast (i.e. with high strain rate), the buckling mode does not follow the shape of the first bending mode of the $SLMoS_2$, and there will be more ripples in the buckling $SLMoS_2$. In other words, higher-energy bending modes are actuated by the fast compression.

This strain rate effect can be interpreted in terms of the relaxation time for each bending mode. The first bending mode has the longest relaxation time (or oscillation period), $\tau = 2\pi/\omega$, due to its lowest angular frequency ω. It means that the longest response time is needed for the appearance of the first bending mode during the compression of the $SLMoS_2$. When the system is compressed very fast, the response time is too short for the appearance of the first bending mode. Instead, higher-energy bending modes have shorter relaxation time, and are able to be actuated by buckling when the $SLMoS_2$ is subjected to a fast compression.

Fig. 3 shows the buckling critical strain for $SLMoS_2$ of different length. The system is compressed at three different strain rates. The simulation data are fitted to the function $\epsilon_c = a + bn_x^{-2}$. The second term n_x^{-2} obeys the Euler buckling theory, which says that the critical strain is an inverse quadratic function of the system length[1]. It means that the Euler buckling theory is valid for short systems. However, in the limit of $n_x \to +\infty$, the critical strain becomes a length-independent constant a = 0.0198, 0.0060, and 0.0015 for strain rates of 10^9 s^{-1}, 10^8 s^{-1}, and 10^7 s^{-1}, respectively. This saturating phenomenon clearly demonstrates that the Euler buckling theory is not applicable in such dynamical process. For $\dot{\epsilon} = 10^7$ s^{-1}, the critical strain is almost saturate when $n_x > 100$. For higher strain rates, the saturation of the critical strain happens at shorter length. More specifically, the critical strain becomes a constant when $n_x > 50$ for $\dot{\epsilon} = 10^8$ s^{-1}, and $n_x > 15$ for $\dot{\epsilon} = 10^9$ s^{-1}. The fitting parameter a becomes closer to zero for lower strain rate, as the dynamical process is more similar as a static process when the strain rate is lower.

To explore the origin for the inapplicability of the Euler buckling theory, we examine the ripples in the buckling mode. We first count the number of ripples in the buckling mode. For $\dot{\epsilon} = 10^7$ s^{-1}, there is only one ripple in the buckled $SLMoS_2$ with $n_x < 100$. For $\dot{\epsilon} = 10^8$ s^{-1}, the buckled $SLMoS_2$ has only one ripple if $n_x < 50$. For $\dot{\epsilon} = 10^9$ s^{-1}, there is only one ripple in the buckled $SLMoS_2$ with $n_x < 15$, and more ripples are observed for longer systems with $n_x >$ 15. For instance, the insets of Fig. 2 show that there are many ripples in the buckled $SLMoS_2$ with n_x = 100, when this system is compressed at a strain rate of 10^9 s^{-1}. These ripples are utilized to get the averaged ripple size. It should be noted that, for short systems with only one ripple in the buckling mode, the length of the $SLMoS_2$ will be regarded as the averaged ripple size, and the error is simply chosen as 10% of the length in this situation.

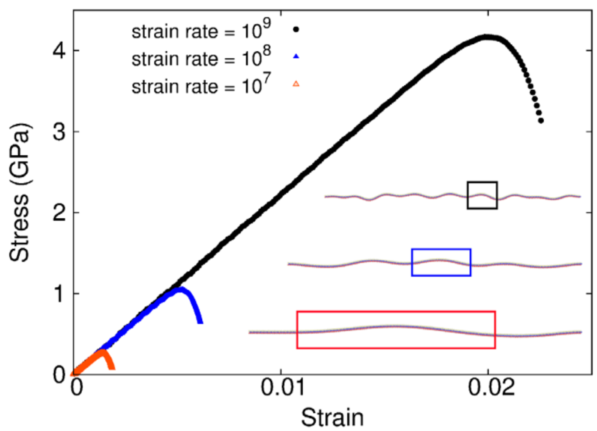

Figure 2 | **Strain rate effect on the buckling critical strain of $SLMoS_2$ with n_x = 100.** Insets (from top to bottom) illustrate the buckling mode of the $SLMoS_2$ at strain rates of 10^9 s^{-1}, 10^8 s^{-1}, and 10^7 s^{-1}, respectively. The size of a single buckling ripple is enclosed by the rectangular.

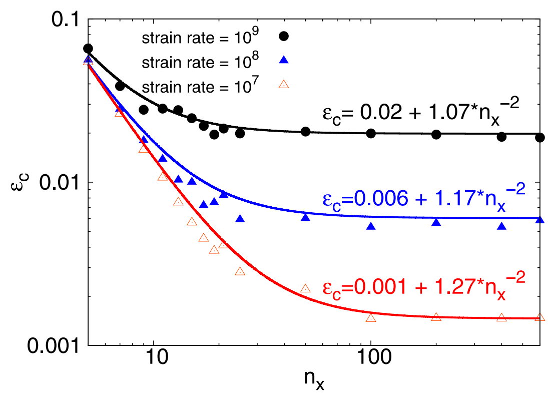

Figure 3 | **Length dependence (log-log) of the buckling critical strain for the $SLMoS_2$ at strain rates of 10^9 s^{-1}, 10^8 s^{-1}, and 10^7 s^{-1}, respectively.** Simulated data are fitted to the function $\epsilon_c = a + bn_x^{-2}$, which becomes a length-independent constant a in the limit of $n_x \to +\infty$.

Fig. 4 shows the length dependence of the averaged ripple size for $SLMoS_2$, which is compressed at different strain rates. The inset of Fig. 4 shows the distribution of the ripple size for a buckling $SLMoS_2$ with $n_x = 600$, which is compressed at $\dot{\epsilon} = 10^8$ s^{-1}. Twenty good ripple samples have been picked out from the buckled $SLMoS_2$ for the production of this histogram plot. The averaged ripple size from the histogram figure is $\lambda = 90.7 \pm 3.3$ Å. Fig. 4 shows an interesting phenomenon that the averaged ripple size is almost saturated for longer systems with larger n_x, where more ripples appear. For higher strain rate, the averaged ripple size becomes saturated at smaller length. This saturation phenomenon is similar as the length dependence of the buckling critical strain shown in Fig. 3, which has demonstrated the inapplicability of the Euler buckling theory.

To further understand the saturation phenomenon shown in Fig. 4, we compute the frequency dispersion for the bending wave using the same Stillinger-Weber potential. The obtained relation between the frequency (f) and the wave vector along the armchair direction (k) is $f = 8.6 \times 10^{12} k^2$ s^{-1}. The bending wave is a exural mode for the quasi-two-dimensional $SLMoS_2$ system, so its frequency is a quadratic function of the wave vector k. The wave vector is an inverse proportional function of the length, i.e., $k \propto L^{-1}$, with $L = n_x \times 5.40$ Å as the length in the armchair direction. As a result, we have $f = 8.6 \times 10^{12} L^{-2}$ s^{-1}.

We take the strain rate $\dot{\epsilon} = 10^9$ s^{-1} as an example. For this strain rate, there are two major findings in Fig. 4. First, the lowest-frequency bending motion is excited for short system with $n_x = 10$; while this lowest-frequency bending motion is not excited for long system with $n_x = 100$. This can be explained by the interplay between the strain rate and the bending frequency. A compression can only excite the bending motion with frequency higher than the strain rate for this compression. For $n_x = 10$, the frequency of the bending wave is around $f \approx 2.9 \times 10^9$ s^{-1} according to the above formula. This frequency is larger than the strain rate. It means that a strain rate of $\dot{\epsilon} = 10^9$ s^{-1} is slow enough to excite the lowest-frequency bending motion in this system. However, for $n_x = 100$, the frequency of the bending wave is around $f \approx 2.9 \times 10^7$ s^{-1}, which is about two orders smaller than the strain rate. As a result, a strain rate of $\dot{\epsilon} = 10^9$ s^{-1} is too fast to allow the the appearance of the lowest-frequency bending motion. Second, it can be seen in Fig. 4 that the saturated value for the ripple size is about $\lambda = 50$ Å. The frequency for the bending wave according to this length is about $f \approx 3.4 \times 10^9$ s^{-1}, which is on the same order as the strain rate. As a result, the saturated ripple size can be excited by a strain rate of $\dot{\epsilon} = 10^9$ s^{-1}.

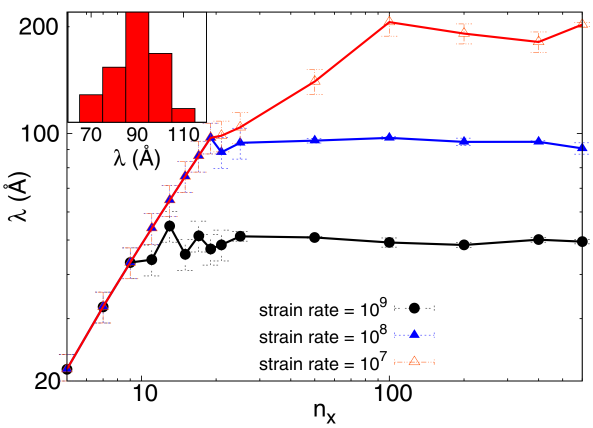

Figure 4 | The log-log plot for the length dependence of the average ripple size (λ) for $SLMoS_2$ compressed by strain rates of 10^9 s^{-1}, 10^8 s^{-1}, and 10^7 s^{-1}, respectively. Inset shows the distribution of the ripple size for a buckling $SLMoS_2$ with $n_x = 600$, which is compressed at $\dot{\epsilon} = 10^8$ s^{-1}. Twenty good ripple samples have been picked out from the buckled $SLMoS_2$ for the production of this histogram plot. The averaged ripple size from the histogram figure is $\lambda = 90.7 \pm 3.3$ Å. Lines are guide to the eye.

Inspired by the saturation phenomena in both Figs. 3 and 4, we find that the Euler buckling theory is closely related to the number of ripples in the buckling mode. It is valid only if one ripple is actuated in the buckling mode. However, the Euler buckling theory becomes invalid when more ripples appear. The Euler buckling theory says[1],

$$\epsilon_c = -\frac{4\pi^2 D}{C_{11} L^2} = -\frac{43.52}{L^2}, \tag{1}$$

where L is the length of the system. We have used the Stillinger-Weber potential to extract the bending modulus[17] $D = 9.61$ eV and the in-plane tension stiffness[16] $C_{11} = 139.5$ Nm^{-1} for the $SLMoS_2$. We note an important fact that only one ripple is assumed in the buckling mode during the derivation of Eq. (1). However, Fig. 4 discussed the suitability of the Euler buckling theory with L as the total length of the system. It seems that a more proper way is to treat L in Eq. (1) as the size of an individual ripple in the buckling mode with many ripples. We thus show the relation between the buckling critical strain and the averaged ripple size in Fig. 5. The prediction of the Euler buckling theory is also plotted in the figure (black solid line) for comparison. We find that all simulation data (calculated with different strain rates) are closely distributed around the line for the Euler buckling theory. In other words, the Euler buckling theory is applicable and is independent of the strain rate, after we treat L in Eq. (1) as the averaged ripple size. The merit of using lower strain rate (10^7 s^{-1}) is to extend the examination of the Euler buckling theory to larger ripple size.

Discussions

We have performed MD simulations to investigate whether the Euler buckling theory is applicable for dynamical processes, in which the $SLMoS_2$ is compressed at high strain rates. We found that the theory is not applicable in the presence of many ripples in the buckling mode, where the buckling critical strain becomes a length-independent constant. However, we have also showed that the Euler buckling theory becomes applicable if this theory is applied to a single ripple in the buckled $SLMoS_2$.

Methods

MD simulation details. All MD simulations in this work are performed using the publicly available simulation code LAMMPS[23], while the OVITO package was used

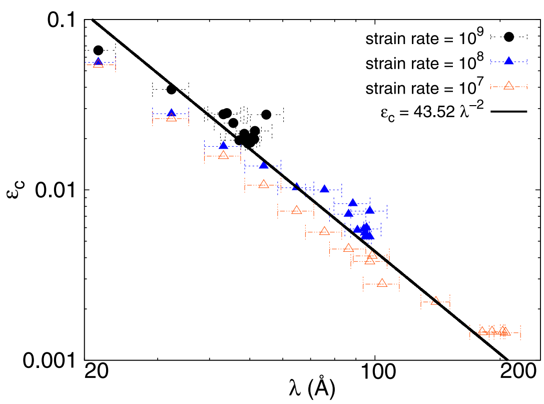

Figure 5 | The log-log plot for the buckling critical strain versus the averaged buckling ripple size for $SLMoS_2$ compressed by strain rates of 10^9 s^{-1} s^{-1}, 10^8 s^{-1} s^{-1}, and 10^7 s^{-1}, respectively. The solid line is the prediction of the Euler buckling theory. All simulation data are close to the solid line, which validates the Euler buckling theory after using the averaged ripple size.

for visualization[24]. The standard Newton equations of motion are integrated in time using the velocity Verlet algorithm with a time step of 1 fs. The interaction within MoS_2 is described by the Stillinger-Weber potential[16]. All simulations are performed at 1.0 K low temperature, so that our MD simulations are more comparable with the Euler buckling theory, which does not consider the temperature effect. The $SLMoS_2$ is thermalized using the Nosé-Hoover[25,26] thermostat for 100 ps within the NPT (i.e. the number of particles N, the pressure P and the temperature T of the system are constant) ensemble. After thermalization, the $SLMoS_2$ is compressed along the armchair direction, while the system is allowed to be fully optimized in the zigzag direction. The NPT ensemble is also applied in the compression step.

1. Timoshenko, S. & Woinowsky-Krieger, S. *Theory of Plates and Shells, 2nd ed* (McGraw-Hill, New York, 1987).
2. Jiang, J.-W., Leach, A. M., Gall, K., Park, H. S. & Rabczuk, T. A surface stacking fault energy approach to predicting defect nucleation in surface-dominated nanostructures. *J. Mech. Phys. Solids* **61**, 1915–1934 (2013).
3. Kam, K. K. & Parkinson, B. A. Detailed photocurrent spectroscopy of the semiconducting group vi transition metal dichalcogenides. *J. Phys. Chem.* **86**, 463–467 (1982).
4. Wang, Q. H., Kalantar-Zadeh, K., Kis, A., Coleman, J. N. & Strano, M. S. Electronics and optoelectronics of two-dimensional transition metal dichalcogenides. *Nat. Nanotechnol.* **7**, 699–712 (2012).
5. Chhowalla, M. *et al.* The chemistry of two-dimensional layered transition metal dichalcogenide nanosheets. *Nat. Chem.* **5**, 263–275 (2013).
6. Castellanos-Gomez, A. *et al.* Elastic properties of freely suspended mos_2 nano sheets. *Adv. Mater.* **24**, 772–775 (2012).
7. Castellanos-Gomez, A. *et al.* Mechanical properties of freely suspended semiconducting graphene-like layers based on mos2. *Nanoscale Res. Lett.* **7**, 1–7 (2012).
8. Huang, W., Da, H. & Liang, G. Thermoelectric performance of mx_2 (m = mo, w; x = s, se) monolayers. *J. Appl. Phys.* **113**, 104304 (2013).
9. Bertolazzi, S., Brivio, J. & Kis, A. Stretching and breaking of ultrathin mos_2. *ACS Nano* **5**, 9703–9709 (2011).
10. Cooper, R. C. *et al.* Nonlinear elastic behavior of two-dimensional molybdenum disulfide. *Phys. Rev. B* **87**, 035423 (2013).
11. Cooper, R. C. *et al.* Erratum: Nonlinear elastic behavior of two-dimensional molybdenum disulfide (physical review b - condensed matter and materials physics(2013) 87 (035423)). *Phys. Rev. B* **87**, 079901 (2013).
12. Varshney, V. *et al.* Md simulations of molybdenum disulphide (mos_2): Force-field parameterization and thermal transport behavior. *Comp. Mater. Sci.* **48**, 101–108 (2010).
13. Liu, X., Zhang, G., Pei, Q.-X. & Zhang, Y.-W. Phonon thermal conductivity of monolayer mos2 sheet and nanoribbons. *Appl. Phys. Lett.* **103**, 133113 (2013).
14. Castellanos-Gomez, A. *et al.* Local strain engineering in atomically thin mos_2. *Nano Lett.* **13**, 5361–5366 (2013).
15. Jiang, J.-W., Zhuang, X.-Y. & Rabczuk, T. Orientation dependent thermal conductance in single-layer mos_2. *Sci. Rep.* **3**, 2209 (2013).
16. Jiang, J.-W., Park, H. S. & Rabczuk, T. Molecular dynamics simulations of single-layer molyb-denum disulphide (mos_2): Stillinger-weber parametrization, mechanical properties, and thermal conductivity. *J. Appl. Phys.* **114**, 064307 (2013).
17. Jiang, J.-W., Qi, Z., Park, H. S. & Rabczuk, T. Elastic bending modulus of single-layer molybdenum disulphide (mos_2): Finite thickness effect. *Nanotechnology* **24**, 435705 (2013).
18. Jiang, J.-W., Park, H. S. & Rabczuk, T. Mos_2 nanoresonators: Intrinsically better than graphene? *Nanoscale* **6**, 3618 (2013).
19. Jiang, J.-W. The buckling of single-layer mos_2 under uniaxial compression. *Nanotechnology* **25**, 355402 (2014).
20. Britnell, L. *et al.* Strong light-matter interactions in heterostructures of atomically thin films. *Science* **340**, 1311–1314 (2013).
21. Bao, W. *et al.* Controlled ripple texturing of suspended graphene and ultrathin graphite membranes. *Nat. Nanotechnol.* **4**, 562–566 (2009).
22. Neek-Amal, M. & Peeters, F. M. Graphene nanoribbons subjected to axial stress. *Phys. Rev. B* **82**, 085432 (2010).
23. Plimpton, S. J. Fast parallel algorithms for short-range molecular dynamics. *J. Comput. Phys.* **117**, 1–19 (1995).
24. Stukowski, A. Visualization and analysis of atomistic simulation data with ovito - the open visualization tool. *Model. Simul. Mater. Sci. Eng.* **18**, 015012 (2010).
25. Nose, S. A unified formulation of the constant temperature molecular dynamics methods. *J. Chem. Phys.* **81**, 511 (1984).
26. Hoover, W. G. Canonical dynamics: Equilibrium phase-space distributions. *Phys. Rev. A* **31**, 1695 (1985).

Acknowledgments

The author thanks T.-Z. Zhang and X.-M. Guo at Shanghai Institute of Applied Mathematics and Mechanics for insightful discussions. The work is supported by the Recruitment Program of Global Youth Experts of China and the start-up funding from Shanghai University.

Author contributions

J.W.J. designed the project, performed the calculations and wrote the paper.

Additional information

Competing financial interests: The authors declare no competing financial interests.

How to cite this article: Jiang, J.-W. The Strain Rate Effect on the Buckling of Single-Layer MoS_2. *Sci. Rep.* **5**, 7814; DOI:10.1038/srep07814 (2015).